

Engineering Non-Hermitian Skin Effect with Band Topology in Ultracold Gases

Lihong Zhou,¹ Haowei Li,^{2,3} Wei Yi,^{2,3,*} and Xiaoling Cui^{1,4,†}

¹*Beijing National Laboratory for Condensed Matter Physics,*

Institute of Physics, Chinese Academy of Sciences, Beijing 100190, China

²*CAS Key Laboratory of Quantum Information, University of Science and Technology of China, Hefei 230026, China*

³*CAS Center For Excellence in Quantum Information and Quantum Physics, Hefei 230026, China*

⁴*Songshan Lake Materials Laboratory, Dongguan, Guangdong 523808, China*

(Dated: January 20, 2022)

Non-Hermitian skin effect (NHSE) describes a unique non-Hermitian phenomenon that all eigenmodes are localized near the boundary, and has profound impact on a wide range of bulk properties. In particular, topological systems with NHSE have stimulated extensive research interests recently, given the fresh theoretical and experimental challenges therein. Here we propose a readily implementable scheme for achieving NHSE with band topology in ultracold gases. Specifically, the scheme realizes the one-dimensional optical Raman lattice with two types of spin-orbit coupling (SOC) and an additional laser-induced dissipation. By tuning the dissipation and the SOC strengths, NHSE and band topology can be individually controlled such that they can coexist in a considerable parameter regime. To identify the topological phase in the presence of NHSE, we have restored the bulk-boundary correspondence by invoking the non-Bloch band theory, and discussed the dynamic signals for detection. Our work serves as a guideline for engineering topological lattices with NHSE in the highly tunable environment of cold atoms, paving the way for future studies of exotic non-Hermitian physics in a genuine quantum many-body setting.

Introduction. Open quantum systems undergoing particle or energy loss can be effectively described by non-Hermitian Hamiltonians. They exhibit intriguing non-Hermitian phenomena that are absent in their Hermitian counterparts, and have thus attracted significant attention in recent years [1, 2]. An outstanding example here is the non-Hermitian skin effect (NHSE) [3–20], under which all bulk eigenstates are localized near the boundary. While NHSE is topologically protected by the winding of eigen-spectrum in the complex energy plane [12, 13], the spectrum itself is sensitive to the actual boundary condition. For instance, both the eigen-spectrum and eigen-wavefunction can be dramatically different under an open boundary condition (OBC) from those under a periodic boundary condition (PBC). A remarkable consequence is the failure of conventional bulk-boundary correspondence in topological systems with NHSE, whose restoration calls for the so-called non-Bloch band theory by employing a generalized Brillouin zone (GBZ) [3–6]. Apart from the fundamental impact on band topology, NHSE can strongly influence many other bulk properties such as the dynamics [9, 16, 21–23], the parity-time symmetry [24, 25] and localization [26, 27].

To date, NHSE has been observed in various non-Hermitian one-dimensional (1D) topological systems including photonics [28–30], topoelectrical circuits [31], and metamaterials [32], wherein the non-Bloch bulk-boundary correspondence has also been confirmed [28, 29, 31]. In these studies, NHSE is predominantly achieved through non-reciprocal hopping, by simulating either the Hatano-Nelson model [33] or the non-reciprocal Su-Schrieffer-Heeger model [3]. At the moment, the study of NHSE deserves a substantial extension to a broader context. On one hand, the appearance of NHSE

is not limited to these models. For instance, a simple spin rotation in momentum space can directly convert the non-reciprocal hopping to on-site dissipation [3, 34], under which NHSE persists [7, 9, 14–16]. On the other hand, given the existing experiments are either classical or on the level of single photons, it is desirable to engineer NHSE in a quantum many-body setting, which would offer exciting opportunities for investigating the interplay of NHSEs with many-body statistics and interactions.

Ultracold atomic gases, with highly controllable parameters, are an ideal candidate for the task. In this platform, through the photon-mediated Raman coupling technique, both the 1D and 2D spin-orbit couplings (SOC) have been realized [35–43], culminating in the successful generation of topological bands in optical lattices [1, 42–45]. Meanwhile, laser-induced atom loss has enabled the experimental realization of parity-time symmetry in ultracold atoms [2, 47, 48], and a very recent experiment manages to incorporate the SOC with laser-induced loss in a single setup [2].

In light of these achievements, we propose to engineer NHSE with band topology in ultracold atoms by utilizing the Raman-assisted SOCs and laser-induced atom loss. Specifically, we consider a one-dimensional optical Raman lattice with two distinct types of SOCs, where the non-trivial band topology derives from the SOCs, and the onset of NHSE relies on the interplay of SOCs and the laser-induced loss. This enables us to independently control NHSE and band topology via the loss rate and SOC strengths. As all aspects of our proposal are readily accessible, our work represents a significant step toward the observation of NHSEs and the associated exotic phenomena in a genuine quantum many-body setting.

Model. As illustrated in Fig. 1, we consider a two-

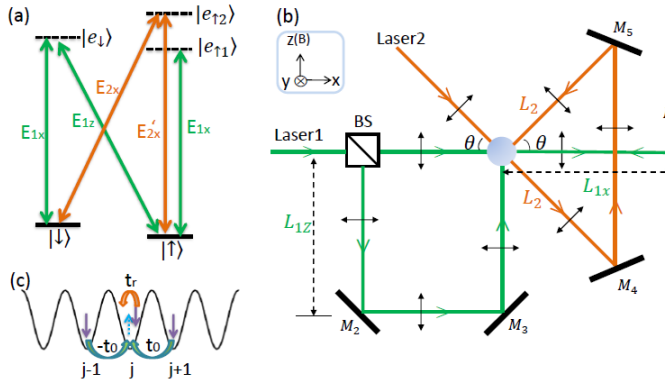


FIG. 1. (Color online) Schematics of the experimental setup in generating two types of SOCs. (a) Two sets of Raman lasers couple the ground spin states via electronically excited states (dashed). (b) Laser configuration and optical-path diagram. The green and orange lines show the propagation directions of the two sets of lasers in (a), and the black arrows indicate their polarizations. L_{1x} , L_{1z} and L_2 are, respectively, the optical paths from the sample to mirror M_1 , from the beam splitting (BS) to M_2 , and from the sample to M_4 (and M_5). The optical lattice potential and the Ω_0 -SOC are generated by $(\mathbf{E}_{1x}, \mathbf{E}_{1z})$, and the Ω_r -SOC is created by $(\mathbf{E}_{2x}, \mathbf{E}'_{2x})$. (c) The Ω_0 - and Ω_r -SOCs respectively generate the nearest-neighbor and the on-site spin flip with tunable strengths $\Omega_0 e^{i\phi_0} (-1)^j$ and $\Omega_r e^{i\phi_r j}$ (j is the site index).

component (\uparrow, \downarrow) atomic gas in a 1D optical lattice (along x), described by the Hamiltonian $H = \int dx H(x)$, with

$$H(x) = \frac{p_x^2}{2m} - V_0 \cos(2k_0 x) + M_0 \sin k_0 x (e^{i\phi_0} \sigma_+ + H.c.) + M_r (e^{i2k_r x} \sigma_+ + h.c.) + i\gamma \sigma_z. \quad (1)$$

Here $\sigma_{\pm} = \sigma_x \pm i\sigma_y$, with σ_{α} ($\alpha = x, y, z$) the Pauli matrices, and $\frac{p_x^2}{2m}$ is the kinetic term.

The optical Raman lattice [1, 42, 43], characterized by V_0 and M_0 , is generated by two Raman lasers: a standing wave propagating along x with the electric-field vector $\mathbf{E}_{1x} = \mathbf{e}_z 2E_{1x} e^{i\phi_{1+}} \cos(k_0 x + \phi_{1-})$, where $\phi_{1\pm} = (\phi_{1x} \pm \phi'_{1x})/2$, and ϕ_{1x} (ϕ'_{1x}) is the phase of incident (reflected) light; and a plane wave propagating along z with $\mathbf{E}_{1z} = \mathbf{e}_x E_{1z} e^{ik_0 z + \phi_{1z}}$. As shown in Fig. 1(b), E_{1x} and E_{1z} come from the same laser source (laser 1) through a beam splitter (BS), enabling an easy manipulation of various relative phases. For instance, the phase $\phi_{1-} (= -k_0 L_{1x})$ is adjustable through the optical path L_{1x} from the sample (grey dot) to mirror M_1 . By taking $\phi_{1-} = -\pi/2$ and $z = 0$, the field \mathbf{E}_{1x} generates a lattice potential with spacing $a = \pi/k_0$ and lattice sites at $x_i = ia$. \mathbf{E}_{1x} , \mathbf{E}_{1z} combine to form the SOC that couples different spins with amplitude $M_0 \sin(k_0 x)$ and phase $\phi_0 = \phi_{1+} - \phi_{1z}$. The phase $\phi_0 = k_0(L_{1x} - 2L_{1z})$ is tunable through L_{1x} or L_{1z} , with L_{1z} the perpendicular distance (along \hat{z}) between the mirrors M_2 , M_3 and the sample.)

An additional SOC, characterized by M_r and known as the equal Rashba and Dresslehaus coupling [35–39, 44, 45], is created by two plane-wave Raman lasers ($\mathbf{E}_{2x}, \mathbf{E}'_{2x}$) with opposite wave-vectors along x and equal phase. As shown in Fig. 1(b), \mathbf{E}_{2x} and \mathbf{E}'_{2x} are both from the laser source 2 (with wave-vector k_0) and intersect at the sample following reflections by two mirrors M_4, M_5 . By adjusting the angle θ between their propagation directions and \hat{x} , the recoil momentum in (1) is tunable as $k_r = k_0 \cos \theta$. Their relative phase can be tuned to zero, as is the case with (1), by adjusting the optical path L between the mirrors and the sample such that $2k_0 L_2 (1 + \sin \theta) = 2n\pi$, with $n \in \mathbb{Z}$.

A laser-induced loss term, characterized by γ , is generated by coupling spin- \downarrow atom to an excited state that is subsequently lost from the system due to spontaneous emission [2, 47, 48]. The conditional dynamics of the system under post-selection is characterized by the non-Hermitian Hamiltonian (1), after dropping the global loss term ($\sim i\gamma$).

The tight-binding model corresponding to Eq.(1) is [50]

$$H = -t \sum_j (c_{j\uparrow}^\dagger c_{j+1\uparrow} + c_{j\downarrow}^\dagger c_{j+1\downarrow} + h.c.) + \Omega_0 \sum_j [e^{i\phi_0} (-1)^j (c_{j\uparrow}^\dagger c_{j+1\downarrow} - c_{j\uparrow}^\dagger c_{j-1\downarrow}) + h.c.] + \Omega_r \sum_j (e^{i\phi_r j} c_{j\uparrow}^\dagger c_{j\downarrow} + h.c.) + i\gamma \sum_j (c_{j\uparrow}^\dagger c_{j\uparrow} - c_{j\downarrow}^\dagger c_{j\downarrow}). \quad (2)$$

Here the two SOCs respectively provide the nearest-neighbor and the on-site spin flip with amplitudes Ω_0 and Ω_r . We henceforth denote them as the Ω_0 - and Ω_r -SOC, respectively, along with the phase parameters $\phi_0 (= \phi_{1+} - \phi_{1z})$ and $\phi_r (= 2\pi k_r/k_0)$. Since all the parameters in (2) are highly tunable, in this work we fix the hopping rate t as the energy unit ($t = 1$) and take $\phi_0, \phi_r \in [0, 2\pi]$.

NHSE and band topology. To provide insight and highlight the individual role of two SOCs, we consider the following three cases:

Case-I: $\Omega_0 = 0, \Omega_r \neq 0$

This is the lattice version of the continuum gas with non-Hermitian SOC, as implemented recently in Ref. [2]. Here, following the gauge transformation $c_{j\downarrow} \rightarrow c_{j\downarrow} e^{-i\phi_r j}$, we obtain the Bloch Hamiltonian $H(k) = -2t \cos(\phi_r/2) \cos \tilde{k} + \Omega_r \sigma_x + (i\gamma - 2t \sin(\phi_r/2) \sin \tilde{k}) \sigma_z$ (with $\tilde{k} = k + \phi_r/2$) and the eigenenergy

$$E_{k\pm}^{(I)} = -2t \cos(\phi_r/2) \cos \tilde{k} \pm \sqrt{\Omega_r^2 + (i\gamma - 2t \sin(\phi_r/2) \sin \tilde{k})^2}. \quad (3)$$

The eigenspectrum supports two exceptional points at $\Omega_r = \gamma$, when $\tilde{k} = 0, \pi$ or $\phi_r = 0$.

Importantly, the system hosts NHSE for $\phi_r \neq 0, \pi$, as clearly indicated by the closed-loop topology [12, 13] of

(3) in the complex plane. The presence of NHSE leads to distinct spectra under PBC and OBC, and localized bulk eigen-modes near the OBC boundary (see Fig. 2 (a2,b2)). Nevertheless, this case is trivial in band topology, since $H(k)$ does not show any spin-winding as k traverses the Brillouin zone. As a result, the OBC spectrum does not feature any in-gap topological modes (see Fig. 2 (a1,a2)).

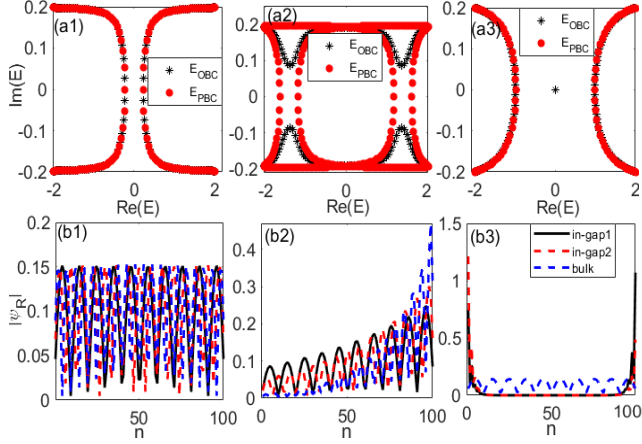


FIG. 2. (Color online) Eigenspectrum (a1-a3) and spatial profile of eigen-modes (b1-b3) for case-I and -II when only one of the SOCs is present. Here we take $\gamma = 0.2$, and (a1,b1) $(\Omega_0, \phi_0, \Omega_r, \phi_r) = (0, -0.3, \pi)$; (a2,b2) $(\Omega_0, \phi_0, \Omega_r, \phi_r) = (0, -0.3, \pi/2)$; (a3,b3) $(\Omega_0, \phi_0, \Omega_r, \phi_r) = (0.5, \pi/2, 0, -)$. NHSE shows up only in (a2,b2). (a3,b3) is topological with two in-gap zero-modes localized at both boundaries.

Case-II: $\Omega_0 \neq 0, \Omega_r = 0$

This is the case with only optical Raman lattice and dissipation. Following the transformation $c_{j\downarrow} \rightarrow (-1)^j c_{j\downarrow}$, the Bloch Hamiltonian $H(k) = 2\Omega_0 \sin k (\sin \phi_0 \sigma_x + \cos \phi_0 \sigma_y) + (i\gamma - 2t \cos k) \sigma_z$, and the eigenspectrum is

$$E_{k\pm}^{(II)} = \pm \sqrt{(2\Omega_0 \sin k)^2 + (i\gamma - 2t \cos k)^2}. \quad (4)$$

Clearly, there is no NHSE — the spectrum (4) exhibits no loop structures in the complex plane. However, $H(k)$ possesses non-trivial band topology, as further confirmed in Fig. 2 (a3,b3) by the appearance of in-gap zero modes under OBC and their localized wave functions near boundaries. The topological transition occurs at $\gamma = 2\Omega_0$ for all ϕ_0 , when the band gap closes at $k = \pi/2, 3\pi/2$. We note that the topological phase of a similar model under a real Zeeman field ($i\gamma \rightarrow \Gamma_z$) and $\phi_0 = 0$ has been studied in Ref. [51], where the topological transition occurs at $\Gamma_z = 2t$.

One can see that the Ω_r -SOC and the Ω_0 -SOC can respectively give rise to NHSE and band topology, as they respectively lead to spectral and wave-function windings. In order to achieve both in a single setting, one needs to incorporate all essential gradients to satisfy both winding conditions. A natural contender is by combining both types of SOCs, as well as the on-site loss.

Case-III: $\Omega_0 \neq 0, \Omega_r \neq 0$

When both types of SOCs are switched on, an analytical form of the eigenspectrum is generally unavailable. An exception is when $\phi_r = \pi$, under which the two SOCs are commensurate and k is still a good quantum number. The Bloch Hamiltonian is $H(k) = (\Omega_r + 2\Omega_0 \sin \phi_0 \sin k) \sigma_x + 2\Omega_0 \cos \phi_0 \sin k \sigma_y + (i\gamma - 2t \cos k) \sigma_z$, with the eigenspectrum

$$E_{k\pm}^{(\text{III}, \phi_r=\pi)} = \pm \left[(\Omega_r^2 + (2\Omega_0 \sin k)^2 + 4\Omega_r \Omega_0 \sin \phi_0 \sin k + (i\gamma - 2t \cos k)^2 \right]^{1/2}. \quad (5)$$

We see immediately that once $\phi_0 \neq 0, \pi$, the spectrum (5) would form a loop in the complex plane, signifying the presence of NHSE. Moreover, $H(k)$ in this case keeps a similar spin winding pattern as in case-II, and thus the system acquires a band topology. In particular, when $\phi_0 = \pi/2, 3\pi/2$ the system has the chiral symmetry: $\sigma_y H(k) \sigma_y = -H(k)$, which protects the degenerate topological zero modes. In Fig. 3, we have numerically verified the coexistent skin and topological properties for $\phi_r = \pi$ and $\phi_0 = \pi/2$, from both the different eigen-spectra between PBC and OBC (Fig. 3(a)), and the localized bulk state and in-gap zero modes (Fig. 3(b)).

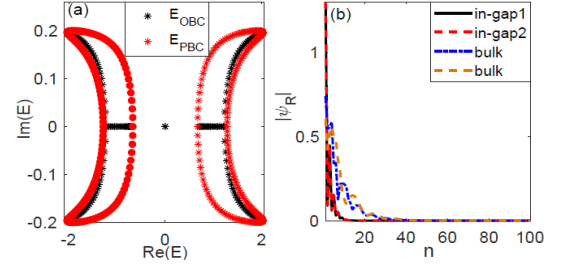


FIG. 3. (Color online) Coexistence of NHSE and band topology for case-III with $\phi_r = \pi, \phi_0 = \pi/2$, and $\Omega_0 = 0.5, \Omega_r = 0.3, \gamma = 0.2$. (a) Energy spectra under PBC and OBC in the complex plane. (b) Spatial wavefunctions for the two topological edge modes and two randomly chosen bulk states.

The band topology can be conveniently tuned by γ and Ω_0, Ω_r . In Fig. 4(a1), we take a specific set of Ω_0 and Ω_r , and show that by increasing γ to a critical γ_c , the in-gap zero modes merge into the bulk and the gap closes and reopens across this critical point. This signifies a topological transition into the trivial phase. Remarkably, γ_c is different from the gap-closing point of the eigen-spectrum (5) under PBC, where $\gamma_{c,\text{PBC}} = |\Omega_r \pm 2\Omega_0|$. This is exactly the breakdown of conventional bulk-boundary correspondence under NHSE.

To restore the bulk-boundary correspondence, we adopt the non-Bloch band theory [3-6] and compute the winding number W in the GBZ[50]. As shown in Fig. 4(a2), W can well predict the topological transition under OBC: the in-gap zero modes emerge where $W = 1$ ($\gamma < \gamma_c$) and vanish where $W = 0$ ($\gamma > \gamma_c$). In fact, γ_c

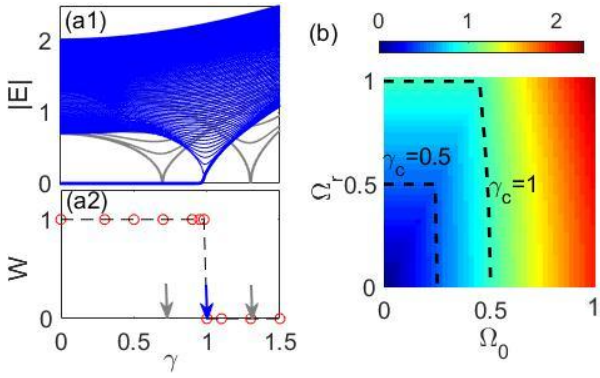


FIG. 4. (Color online) Topological phase transition for case-III with $\phi_r = \pi$, $\phi_0 = \pi/2$. (a1,a2) The amplitude of spectrum $|E|$ under OBC (blue) and the winding number obtained from GBZ as functions of γ . Here we take $\Omega_0 = 0.5$, $\Omega_r = 0.3$. The topological transition occurs at $\gamma_c \sim 1$, which differs from the PBC predictions $\gamma_{c,PBC} = 0.7, 1.3$ (gray arrows). The PBC eigenspectrum is shown in grey for comparison. (b) Contour plot of γ_c in (Ω_0, Ω_r) plane.

can be obtained analytically through the gap-closing condition of the GBZ spectrum [50]. The resulting topological phase diagram is given in Fig. 4 (b), where γ_c is plotted as functions of Ω_0 and Ω_r for the case of $\phi_0 = \pi/2$. The $\phi_0 = 3\pi/2$ case is found to share the same diagram due to symmetries [50].

When (ϕ_r, ϕ_0) deviate from $(\pi, \pi/2)$ and $(\pi, 3\pi/2)$, the chiral symmetry is broken and the topological modes would split and gradually merge into the bulk. In comparison, NHSE is much more robust, which can persist for all (ϕ_r, ϕ_0) except for $\phi_r = 0$ and two discrete points (π, π) and $(\pi, 0)$ [50]. In Table I, we summarize the conditions for band topology and NHSE for cases I-III. A main message is that both SOCs are indispensable in achieving NHSE and topology simultaneously. Moreover, the two SOCs show intriguing interplay effect. For instance, the application of Ω_r -SOC in case III changes the topology condition as compared to case II, and the Ω_0 -SOC changes the skin condition as compared to case I.

		topological	skin	topological + skin
case-I	$\Omega_0 = 0, \Omega_r \neq 0$	\times	$\phi_r \neq 0, \pi$	\times
case-II	$\Omega_0 \neq 0, \Omega_r = 0$	$\gamma < 2\Omega_0$	\times	\times
case-III	$\Omega_0 \neq 0, \Omega_r \neq 0$	$\phi_r = \pi, \phi_0 = \frac{\pi}{2}, \frac{3\pi}{2}$ and $\gamma < \gamma_c$	$\phi_r \neq 0$ and $(\phi_r, \phi_0) \neq (\pi, 0), (\pi, \pi)$	$\phi_r = \pi, \phi_0 = \frac{\pi}{2}, \frac{3\pi}{2}$ and $\gamma < \gamma_c$

TABLE I. Conditions for achieving topological phase and NHSE for various cases. " \times " means absence for all occasions.

Dynamic detection. To detect the topological phase with NHSE, we propose an edge-to-edge transport measurement. In the Hermitian case, the topological edge modes play the dominant role in such transport [52]. However, in the presence of NHSE, the transport is expected to be significantly modified since all bulk modes also localize near the edge. To examine such an effect, we compare two topological systems in our setup, one is Hermitian at $\gamma = 0$, and the other is with NHSE at finite γ . We study the probability of particle occupation at the β -edge of the system at time τ , when the initial state starts from the α -edge ($\alpha, \beta = L$ or R)

$$P_{\alpha\beta}(\tau) = |\langle \beta | e^{-iH\tau} | \alpha \rangle|^2. \quad (6)$$

To eliminate the difference caused by spin, we take the initial state as the equal population of \uparrow and \downarrow and show its dynamics in Fig. 5. In the Hermitian case (Fig. 5 (a)), the left-to-right (P_{LR}) and right-to-left (P_{RL}) transports are identical. As a manifestation of the topological edge states, the oscillation frequency of P_{LR} (or P_{RL}), as given by the energy gap between the two edge modes in a finite-size system, is found to decay exponentially with increasing system size (inset of Fig. 5 (a)). In the presence of NHSE (Fig. 5 (b)), the transport properties

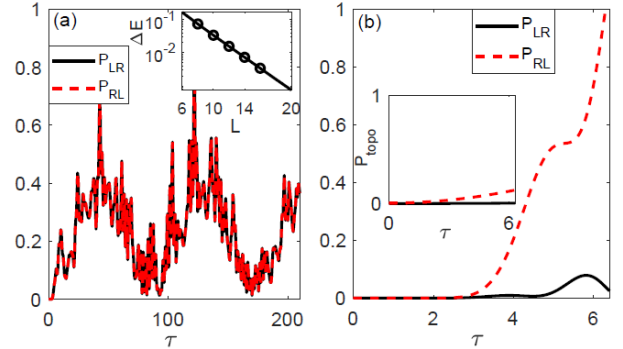


FIG. 5. (Color online) Edge-to-edge transport properties for the topological system without (a) and with (b) NHSE. We take $\Omega_0 = 0.5$, $\Omega_r = 0.3$, and $\gamma = 0$ (a), 0.2 (b). In the main plots, the system size $L = 8$. The inset of (b) shows the contribution from the topological edge states.

are dramatically different. Due to the localization of skin modes at the left boundary, the transport shows strong directional preference towards the left side, namely. In this case, the topological edge modes play little role in affecting the dynamics (inset of Fig. 5 (b)). These fea-

tures distinguish the topological phases with and without NHSE.

Optical lattices with sharp boundaries can be implemented using box-trap potentials [53–57], where the spatial extent of an edge is determined by the optical wavelength $\sim 1\mu\text{m}$ (much smaller than typical trap length $\sim 10\text{--}100\mu\text{m}$). Such a small imperfection does not visibly change the dynamics in Fig. 5 [50]. Alternatively, NHSE can also manifest itself in the bulk dynamics [16, 21, 22] in the form of strong direction bulk transport, even under typical harmonic trapping potentials [50].

Summary and Discussion. We have proposed a realistic scheme in utilizing the SOCs and the spin-dependent dissipation in ultracold atoms to engineer NHSE with band topology. We emphasize that both SOCs are indispensable in the scheme. Their mutual interference, along with their interplay with the on-site dissipation, determine the ultimate parameter regime for skin modes with non-trivial band topology (Table I). Our scheme is applicable to a wide range of alkali and alkali-earth(-like) atoms. A promising candidate is ^{173}Yb , where both the optical Raman lattice with band topology [1] and non-Hermitian SOC [2] have been realized using the Raman-induced $^1S_0 \leftrightarrow ^3P_1$ transitions. A detailed Raman-transition scheme corresponding to Fig. 1(a) for ^{173}Yb can be found in [50].

For future studies, an intriguing possibility would be tuning ϕ_r away from π such that the two SOCs become incommensurate. The competition between quasiperiodicity and NHSE would potentially lead to unique localization features [26, 27]. Further generalization of our scheme to higher dimensions would offer the opportunity for achieving Weyl exceptional rings [58], and high-order skin effect and band topology featuring corner or hinge modes [59–61]. Moreover, the implementation of NHSE in ultracold atoms paves the way for exploring collective phenomena therein due to inter-atomic interactions, which are easily tunable through Feshbach resonances. Our proposal therefore ushers in a wide variety of possibilities for the quantum simulation of non-Hermitian physics.

Acknowledgement. The work is supported by the National Key Research and Development Program of China (2018YFA0307600, 2017YFA0304100), the National Natural Science Foundation of China (No.12074419, No. 11974331), and the Strategic Priority Research Program of Chinese Academy of Sciences (No. XDB33000000).

Hermitian physics and PT symmetry”, Nat. Phys. 14, 11 (2018).

- [2] Y. Ashida, Z. Gong, and M. Ueda, “Non-Hermitian Physics”, Adv. Phys. 69, 3 (2020).
- [3] S. Yao and Z. Wang, “Edge States and Topological Invariants of Non-Hermitian Systems”, Phys. Rev. Lett. 121, 086803 (2018).
- [4] S. Yao, F. Song, and Z. Wang, “Non-Hermitian Chern Bands”, Phys. Rev. Lett. 121, 136802 (2018).
- [5] Z. Yang, K. Zhang, C. Fang, and J. Hu, “Non-Hermitian Bulk-Boundary Correspondence and Auxiliary Generalized Brillouin Zone Theory”, Phys. Rev. Lett. 125, 226402 (2020).
- [6] K. Yokomizo and S. Murakami, “Non-Bloch Band Theory of Non-Hermitian Systems”, Phys. Rev. Lett. 123, 066404 (2019).
- [7] V. M. Martinez Alvarez, J. E. Barrios Vargas, and L. E. F. Foa Torres, “Non-Hermitian robust edge states in one dimension: Anomalous localization and eigenspace condensation at exceptional points”, Phys. Rev. B 97, 121401(R) (2018).
- [8] C. H. Lee and R. Thomale, “Anatomy of skin modes and topology in non-Hermitian systems”, Phys. Rev. B 99, 201103(R) (2019).
- [9] F. Song, S. Yao, and Z. Wang, “Non-Hermitian Skin Effect and Chiral Damping in Open Quantum Systems”, Phys. Rev. Lett. 123, 170401 (2019).
- [10] T.-S. Deng and W. Yi, Phys. Rev. B “Non-Bloch topological invariants in a non-Hermitian domain-wall system”, Phys. Rev. B, 100, 035102 (2019).
- [11] D. S. Borgnia, A. J. Kruchkov, and R.-J. Slager, “Non-Hermitian Boundary Modes and Topology,” Phys. Rev. Lett. 124, 056802 (2020).
- [12] K. Zhang, Z. Yang, and C. Fang, “Correspondence between Winding Numbers and Skin Modes in Non-Hermitian Systems”, Phys. Rev. Lett. 125, 126402 (2020).
- [13] N. Okuma, K. Kawabata, K. Shiozaki, and M. Sato, “Topological Origin of Non-Hermitian Skin Effects”, Phys. Rev. Lett. 124, 086801 (2020).
- [14] Y. Yi and Z. Yang, “Non-Hermitian Skin Modes Induced by On-Site Dissipations and Chiral Tunneling Effect”, Phys. Rev. Lett. 125, 186802 (2020).
- [15] L. Li, C. H. Lee, and J. Gong, “Topological Switch for Non-Hermitian Skin Effect in Cold-Atom Systems with Loss”, Phys. Rev. Lett. 124, 250402 (2020).
- [16] S. Longhi, “Probing non-Hermitian skin effect and non-Bloch phase transitions”, Phys. Rev. Research 1, 023013 (2019).
- [17] S. Longhi, “Non-Bloch-Band Collapse and Chiral Zener Tunneling”, Phys. Rev. Lett. 124, 066602 (2020).
- [18] C.-X. Guo, C.-H. Liu, X.-M. Zhao, Y. Liu, and S. Chen, “Exact Solution of Non-Hermitian Systems with Generalized Boundary Conditions: Size-Dependent Boundary Effect and Fragility of the Skin Effect”, Phys. Rev. Lett. 127, 116801 (2021).
- [19] P. M. Vecsei, M. M. Denner, T. Neupert, and F. Schindler, “Symmetry indicators for inversion-symmetric non-Hermitian topological band structures”, Phys. Rev. B 103, L201114 (2021).
- [20] F. Schindler and A. Prem, “Dislocation non-Hermitian skin effect”, Phys. Rev. B 104, L161106 (2021).
- [21] L. Mao, T. Deng, P. Zhang, “Boundary condition independence of non-Hermitian Hamiltonian dynamics”, Phys. Rev. B 104, 125435 (2021).

* wyiz@ustc.edu.cn

† xl cui@iphy.ac.cn

[1] R. El-Ganainy, K. G. Makris, M. Khajavikhan, Z. H. Musslimani, S. Rotter, and D. N. Chiristodoulides, “Non-

[22] C.-H. Liu, S. Chen, “Information Restraint in Open Quantum Systems”, *Phys. Rev. B* 104, 174305(2021).

[23] C.-H. Liu, K. Zhang, Z. Yang, S. Chen, “Helical damping and dynamical critical skin effect in open quantum systems”, *Phys. Rev. Res.* 2, 043167 (2020).

[24] S. Longhi, “Non-Bloch PT symmetry breaking in non-Hermitian photonic quantum walks”, *Opt. Lett.* 44, 5804 (2019).

[25] L. Xiao, T. Deng, K. Wang, Z. Wang, W. Yi, and P. Xue, “Observation of Non-Bloch PT symmetry and exceptional points”, *Phys. Rev. Lett.* 126, 230402 (2021).

[26] S. Longhi, “Topological phase transition in non-Hermitian quasicrystals”, *Phys. Rev. Lett.* 122, 237601 (2019).

[27] Y. Liu, Y. Wang, X.-J. Liu, Q. Zhou, and S. Chen, “Exact mobility edges, PT-symmetry breaking and skin effect in one-dimensional non-Hermitian quasicrystals”, *Phys. Rev. B* 103, 014203 (2021).

[28] L. Xiao, T. Deng, K. Wang, G. Zhu, Z. Wang, W. Yi, and P. Xue, “Non-Hermitian bulk-boundary correspondence in quantum dynamics”, *Nat. Phys.* 16, 761 (2020).

[29] S. Weidemann, M. Kremer, T. Helbig, T. Hofmann, A. Stegmaier, M. Greiter, R. Thomale, and A. Szameit, “Topological funneling of light”, *Science* 368, 311 (2020).

[30] K. Wang, A. Dutt, Ki Youl Yang, Casey C. Wojcik, Jelena Vučović, and Shanhui Fan, “Generating arbitrary topological windings of a non-Hermitian band”, *Science* 371, 1240 (2021).

[31] T. Helbig, T. Hofmann, S. Imhof, M. Abdelghany, T. Kiessling, L. W. Molenkamp, C. H. Lee, A. Szameit, M. Greiter, and R. Thomale, “Generalized bulk-boundary correspondence in non-Hermitian topoelectrical circuits”, *Nat. Phys.* 16, 747 (2020).

[32] A. Ghatak, M. Brandenbourger, J. van Wezel, and C. Coulais, “Observation of non-hermitian topology and its bulk-edge correspondence in an active mechanical meta-material”, *Proceedings of the National Academy of Sciences* 117, 29561 (2020).

[33] N. Hatano and D. R. Nelson, “Localization transition in non-Hermitian quantum mechanics”, *Phys. Rev. Lett.* 77, 570 (1996).

[34] T. E. Lee, “Anomalous Edge State in a Non-Hermitian Lattice”, *Phys. Rev. Lett.* 116, 133903 (2016).

[35] Y.-J. Lin, K. Jiménez-García and I. B. Spielman, “Spin orbit-coupled Bose Einstein condensates”, *Nature* 471, 83 (2011).

[36] J.-Y. Zhang, S.-C. Ji, Z. Chen, L. Zhang, Z.-D. Du, B. Yan, G.-S. Pan, B. Zhao, Y.-J. Deng, H. Zhai, S. Chen and J.-W. Pan, “Collective Dipole Oscillations of a Spin-Orbit Coupled Bose-Einstein Condensate”, *Phys. Rev. Lett.* 109, 115301 (2012).

[37] P. Wang, Z.-Q. Yu, Z. Fu, J. Miao, L. Huang, S. Chai, H. Zhai and J. Zhang, “Spin-Orbit Coupled Degenerate Fermi Gases”, *Phys. Rev. Lett.* 109, 095301 (2012).

[38] L. W. Cheuk, A. T. Sommer, Z. Hadzibabic, T. Yefsah, W. S. Bakr and M. W. Zwierlein, “Spin-Injection Spectroscopy of a Spin-Orbit Coupled Fermi Gas”, *Phys. Rev. Lett.* 109, 095302 (2012).

[39] C. Qu, C. Hamner, M. Gong, C. Zhang and P. Engels, “Observation of Zitterbewegung in a spin-orbit-coupled Bose-Einstein condensate”, *Phys. Rev. A* 88, 021604(R) (2013).

[40] L. Huang, Z. Meng, P. Wang, P. Peng, S. Zhang, L. Chen, D. Li, Q. Zhou, J. Zhang, “Experimental realization of two-dimensional synthetic spin orbit coupling in ultracold Fermi gases”, *Nat. Phys.* 12, 540 (2016).

[41] Z. Meng, L. Huang, P. Peng, D. Li, L. Chen, Y. Xu, C. Zhang, P. Wang, J. Zhang, “Experimental Observation of a Topological Band Gap Opening in Ultracold Fermi Gases with Two-Dimensional Spin-Orbit Coupling”, *Phys. Rev. Lett.* 117, 235304 (2016).

[42] Z. Wu, L. Zhang, W. Sun, X.-T. Xu, B.-Z. Wang, S.-C. Ji, Y. Deng, S. Chen, X.-J. Liu, and J.-W. Pan, “Realization of two-dimensional spin-orbit coupling for Bose-Einstein condensates”, *Science* 354, 83 (2016).

[43] W. Sun, B.-Z. Wang, X.-T. Xu, C.-R. Yi, L. Zhang, Z. Wu, Y. Deng, X.-J. Liu, S. Chen, and J.-W. Pan, “Highly Controllable and Robust 2D Spin-Orbit Coupling for Quantum Gases”, *Phys. Rev. Lett.* 121, 150401 (2018).

[44] M. Mancini, G. Pagano, G. Cappellini, L. Livi, M. Rider, J. Catani, C. Sias, P. Zoller, M. Inguscio, M. Dalmonte, L. Fallani, “Observation of chiral edge states with neutral fermions in synthetic Hall ribbons”, *Science* 349, 1510 (2015).

[45] B. K. Stuhl, H.-I Lu, L. M. Aycock, D. Genkina, I. B. Spielman, “Visualizing edge states with an atomic Bose gas in the quantum Hall regime”, *Science* 349, 1514 (2015).

[46] B. Song, L. Zhang, C. He, T. F. Jeffrey Poon, E. Hajiyev, S. Zhang, X.-J. Liu, G.-B. Jo, “Observation of symmetry-protected topological band with ultracold fermions”, *Sci. Adv.* 4, eaao4748 (2018).

[47] J. Li, A. K. Harter, J. Liu, L. de Melo, Y. N. Joglekar, and L. Luo, “Observation of parity-time symmetry breaking transitions in a dissipative Floquet system of ultracold atoms”, *Nat. Comm.* 10, 855 (2019).

[48] S. Lapp, J. Ang’ong’aa, F. Alex An, B. Gadway, “Engineering tunable local loss in a synthetic lattice of momentum states”, *New. J. Phys.* 21, 045006 (2019).

[49] Z. Ren, D. Liu, E. Zhao, C. He, K. K. Pak, J. Li, G.-B. Jo, “Topological control of quantum states in non-Hermitian spin-orbit-coupled fermions”, arxiv: 2106.04874.

[50] See more details in the supplementary material.

[51] X. -J. Liu, Z. -X. Liu and M. Cheng, “Manipulating Topological Edge Spins in One-Dimensional Optical Lattice”, *Phys. Rev. Lett.* 110, 076401 (2013).

[52] S. de Léséleuc, V. Lienhard, P. Scholl, D. Barredo, S. Weber, N. Lang, H. P. Büchler, T. Lahaye, and A. Browaeys, “Observation of symmetry-protected topological phase of interacting bosons with Rydberg atoms”, *Science* 365, 775 (2019).

[53] A. L. Gaunt, T. F. Schmidutz, I. Gotlibovych, R. P. Smith, and Z. Hadzibabic, “Bose Einstein Condensation of Atoms in a Uniform Potential”, *Phys. Rev. Lett.* 110, 200406 (2013).

[54] L. Chomaz, L. Corman, T. Biénaimé, R. Desbuquois, C. Weitenberg, S. Nascimbène, J. Beugnon, and J. Dalibard, “Emergence of coherence via transverse condensation in a uniform quasi-two-dimensional Bose gas”, *Nat. Commun.* 6, 6162 (2015).

[55] B. Mukherjee, Z. Yan, P. B. Patel, Z. Hadzibabic, T. Yefsah, J. Struck, and M. W. Zwierlein, “Homogeneous atomic Fermi gases”, *Phys. Rev. Lett.* 118, 123401 (2017).

[56] K. Hueck, N. Luick, L. Sobirey, J. Siegl, T. Lompe, and H. Moritz, “Two-dimensional homogeneous Fermi gases”, *Phys. Rev. Lett.* 120, 060402 (2018).

[57] M. Tajik, B. Rauer, T. Schwegler, F. Cataldini, J. Sabino, F. S. Moller, S.-C. Ji, I. E. Mazets, and J.

Schmiedmayer, “Designing arbitrary one-dimensional potentials on an atom chip”, *Optics Express* 27, 33474 (2019).

[58] Y. Xu, S.-T. Wang and L.-M. Duan, “Weyl exceptional rings in a three-dimensional dissipative cold atomic gas”, *Phys. Rev. Lett.* 118, 045701 (2017).

[59] K. Kawabata, M. Sato, K. Shiozaki, “Higher-order non-Hermitian skin effects”, *Phys. Rev. B* 102, 205118 (2020).

[60] L. Li, C. H. Lee, S. Mu, and J. Gong, “Critical non-Hermitian skin effect”, *Nat. Commun.* 11, 5491 (2020).

[61] W. A. Benalcazar, B. A. Bernveig, and T. L. Hughes, “Quantized electric multipole insulators”, *Science* 357, 61 (2017).

In this Supplementary Material we provide more details on the derivation of tight-binding model, the Raman transition diagram for a specific atomic candidate, the topological transition point, the existence of non-Hermitian skin effect (NHSE) and band topology, and the lattice dynamics under realistic external confinements.

I. Derivation of tight-binding model

To derive the tight-binding model, we expand the field operator $\psi_\sigma(x) = \sum_i \omega_{n=0}(x - x_i) c_{i\sigma}$, where $\omega_{n=0}(x)$ is the lowest-band Wannier function and i is the index of lattice sites. In this way, the second-quantized single-particle Hamiltonian can be reduced to the tight-banding model, with the following parameters:

(1) the nearest-neighbor hopping term

$$t = - \int dx \omega_0(x) \left(\frac{p_x^2}{2m} - V_0 \cos(2k_0 x) \right) \omega_0(x - a). \quad (7)$$

(2) the on-site spin-flip terms

$$t_{\uparrow\downarrow}^j = \int dx \omega_0^*(x - x_j) M_r e^{i2k_r x} \omega_0(x - x_j) \equiv e^{i\phi_r j} \Omega_r, \quad (8)$$

$$t_{\downarrow\uparrow}^j = \int dx \omega_0^*(x - x_j) M_r e^{-i2k_r x} \omega_0(x - x_j) \equiv e^{-i\phi_r j} \Omega_r, \quad (9)$$

where the amplitude $\Omega_r = M_r \int dx \omega_0^2(x) e^{i2k_r x}$, and the corresponding phase $\phi_r = 2k_r a = 2\pi k_r / k_0$. Note that here we pin down the coordinate of the j -site atom as $x_j = ja$, with $a = \pi / k_0$ the lattice spacing.

(3) the nearest-neighbor spin-flip terms

$$t_{\uparrow\downarrow}^{j,j+1} = \int dx \omega_0^*(x - x_j) (M_0 \sin k_0 x e^{i\phi_0}) \omega_0(x - x_{j+1}) \equiv e^{i\phi_0} (-1)^j \Omega_0, \quad (10)$$

$$t_{\uparrow\downarrow}^{j,j-1} = \int dx \omega_0^*(x - x_j) (M_0 \sin k_0 x e^{i\phi_0}) \omega_0(x - x_{j-1}) \equiv -e^{i\phi_0} (-1)^j \Omega_0, \quad (11)$$

where the amplitude $\Omega_0 = M_0 \int dx \omega_0(x) \sin k_0 x \omega_0(x - a)$. Again we have used $x_j = ja$.

Finally we get the tight-binding model as Eq. (2) in the main text.

II. Detailed Raman-transition scheme for ^{173}Yb

We illustrate the implementation of our scheme, using level structures of ^{173}Yb atoms as a concrete example. In previous experiments with ^{173}Yb , both the optical Raman lattice [1] and 1D spin-orbit coupling (SOC) with dissipation (or the non-Hermitian SOC) [2] have been successfully implemented. The Raman transitions in these experiments are between the two hyperfine states in the ground-state 1S_0 manifold ($|\uparrow\rangle = |F = 5/2, m_F = 5/2\rangle$ and $|\downarrow\rangle = |F = 5/2, m_F = 3/2\rangle$), and the excited states with $F' = (7/2, 5/2, 3/2)$ states the 3P_1 manifold. The spin-dependent loss is controlled by a near-resonant transition from $|\downarrow\rangle$ to the excited state $|F', m'_F\rangle = |7/2, 1/2\rangle$. In view of these existing implementations, in Fig. 6 we show a specific Raman transition diagram based on the level structures of ^{173}Yb , for realizing our scheme in Fig. 1(a) of the main text.

Here the choice of two spin states $|\uparrow, \downarrow\rangle$, and the energy levels to create the optical Raman lattice, the M_0 -SOC and the spin-dependent loss are all consistent with [1, 2]. To ensure an independent control on the M_r -SOC (from the M_0 -SOC), we propose to consider the Raman transition to a different excited state, say, $|F', m'_F\rangle = |5/2, 5/2\rangle$, as shown in Fig. 6. A specific atomic transition can be achieved by tuning the laser frequency to match the required atomic energy difference. This can be done by using the acousto-optical modulator (AOM), which is a well-developed technique in existing experiments (see, for instance, Refs. [1, 2]).

III. topological phase transition under non-Hermitian skin effect

Here we derive the topological transition for case-III with $\phi_r = \pi$. The transition point γ_c can be determined by the gap closing of the OBC spectrum.

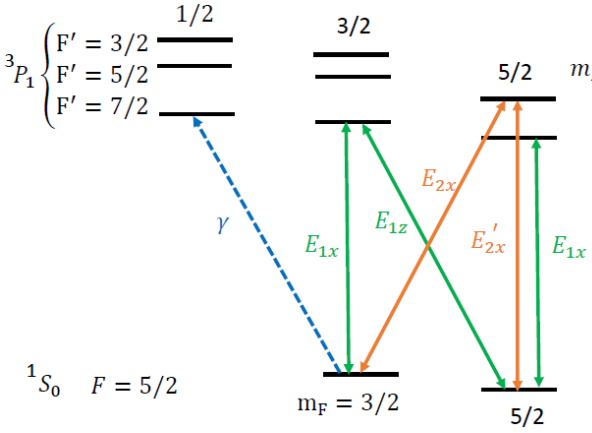


FIG. 6. (Color online) A proposed Raman-transition diagram for ^{173}Yb .

Following the non-Bloch band theory and replacing the vector k by $\beta = e^{ik}$ in the Bloch Hamiltonian, we obtain the non-Bloch Hamiltonian in the spin space as

$$H(\beta) = \begin{pmatrix} i\gamma - t(\beta + \beta^{-1}) & \Omega - e^{i\phi_0} t_{so}(\beta - \beta^{-1}) \\ \Omega + e^{-i\phi_0} t_{so}(\beta - \beta^{-1}) & -i\gamma + t(\beta + \beta^{-1}) \end{pmatrix}. \quad (12)$$

Then the eigenvalues E follow

$$E^2 = [i\gamma - t(\beta + \beta^{-1})]^2 + [\Omega - e^{i\phi_0} t_{so}(\beta - \beta^{-1})](\Omega + e^{-i\phi_0} t_{so}(\beta - \beta^{-1})). \quad (13)$$

For a given value of E , the four solutions of β can be organized as $|\beta_1| \leq |\beta_2| \leq |\beta_3| \leq |\beta_4|$. Imposing the condition $|\beta_2| = |\beta_3|$ would pin down all β -solutions for the generalized Brillouin zone (GBZ). The non-Bloch winding number accumulated in the GBZ is then

$$W = \frac{i}{2\pi} \int_{\beta} \sum_{\nu=\pm} \langle u_{\nu L}(\beta) | \partial_{\beta} | u_{\nu R}(\beta) \rangle, \quad (14)$$

where the right and left eigenvectors are defined through $H(\beta) |u_{\nu R}\rangle = E_{\beta\nu} |u_{\nu R}\rangle$ and $H^{\dagger}(\beta) |u_{\nu L}\rangle = E_{\beta\nu}^* |u_{\nu L}\rangle$. Note that $H(\beta)$ satisfies the chiral symmetry $\sigma_y H(\beta) \sigma_y = -H(\beta)$, for $\phi_0 = \pi/2, 3\pi/2$.

The gap-closing condition, indicative of the topological transition, requires the solution $E = 0$ of (13), i.e.,

$$0 = [i\gamma_c - t(\beta + \beta^{-1})]^2 + [\Omega - e^{i\phi_0} t_{so}(\beta - \beta^{-1})](\Omega + e^{-i\phi_0} t_{so}(\beta - \beta^{-1})). \quad (15)$$

In combination with the continuum band requirement: $|\beta_1| \leq |\beta_2| = |\beta_3| \leq |\beta_4|$, we obtain the relation between γ_c and Ω_0, Ω_r . In particular, since the topological zero modes are protected by the chiral symmetry when $\phi_0 = \pi/2, 3\pi/2$, in the following we shall discuss the topological transition in these two cases separately.

1. $\phi_0 = \pi/2$

The solution of γ_c as a function of Ω_0, Ω_r can be divided to two regimes

$$(1) \quad \text{for } \Omega_0 \leq \Omega_{0c} : \gamma_c = \Omega_r; \quad (16)$$

$$(2) \quad \text{for } \Omega_0 \geq \Omega_{0c} : 2(t\gamma_c + \Omega_r\Omega_0) = (t + \Omega_0)\sqrt{(\Omega_r + \gamma_c)^2 + 4t^2 - 4\Omega_0^2} - (t - \Omega_0)\sqrt{(\Omega_r - \gamma_c)^2 + 4t^2 - 4\Omega_0^2}. \quad (17)$$

Here Ω_{0c} satisfies

$$(t + \Omega_{0c})(\sqrt{\Omega_r^2 + t^2 - \Omega_{0c}^2} - \Omega_r) = (t - \Omega_{0c})\sqrt{t^2 - \Omega_{0c}^2}. \quad (18)$$

2. $\phi_0 = 3\pi/2$

From Eq. (13), we see that the case with $\phi_0 = 3\pi/2$ can be related to that with $\phi_0 = \pi/2$ by the transformation $\beta \rightarrow \beta^{-1}$. This means that we can directly utilize the four β -solutions in $\phi_0 = \pi/2$ case, i.e., $|\beta_1| \leq |\beta_2| = |\beta_3| \leq |\beta_4|$, to obtain the solutions in the $\phi_0 = 3\pi/2$ case as $|\beta_4|^{-1} \leq |\beta_3|^{-1} = |\beta_2|^{-1} \leq |\beta_1|^{-1}$, without any change of the spectrum E . Therefore the topological transition points in the two cases should be identical. We have numerically confirmed that γ_c has the same dependence on the parameters Ω_0, Ω_r as in the case of $\phi_0 = \pi/2$.

IV. Non-Hermitian skin effect and band topology in the general (ϕ_r, ϕ_0) phase plane

Here we discuss the presence of NHSE and band topology in case-III with general phase parameters (ϕ_r, ϕ_0) .

First, we discuss the band topology when the system is away from the points $(\phi_r = \pi, \phi_0 = \pi/2, 3\pi/2)$. In Fig. 7, we show the OBC spectrum by taking the same $(\Omega_0, \Omega_r, \gamma)$ as those in Fig. 3 of the main text, but with two different sets of phase parameters (ϕ_r, ϕ_0) . We see that the topological zero modes are now replaced by two finite-energy in-gap modes.

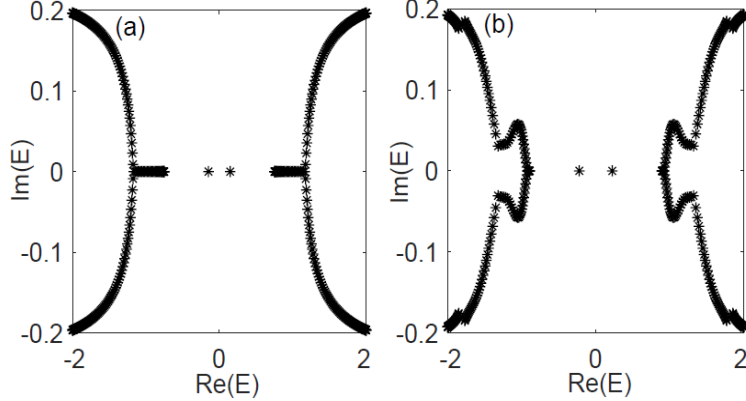


FIG. 7. (Color online) Energy spectrum under the open boundary condition (OBC) for (a) $(\phi_r, \phi_0) = (\pi, \pi/3)$ and (b) $(\phi_r, \phi_0) = (2\pi/3, \pi/2)$. In both cases we take $\Omega_0 = 0.5, \Omega_r = 0.3, \gamma = 0.2$, the same as in Fig. 3 of the main text.

To gain more insight to the vanishing of the topological zero modes under OBC, let us examine the Bloch Hamiltonian $H(k)$ for $\phi_r = \pi$ and $\phi_0 \neq \pi/2, 3\pi/2$. In this case, $H(k)$ develops a σ_y component, and the chiral symmetry is no longer present. We have also verified from the tight-binding model that the chiral symmetry breaks down also for $\phi_r \neq \pi$, and thus the band topology is destroyed as long as (ϕ_r, ϕ_0) deviates from the points $(\pi, \pi/2)$ and $(\pi, 3\pi/2)$.

Finally, the appearance of the NHSE is found to be much more robust as compared to the band topology. We have explained in the main text that for the case $\phi_r = \pi$, the skin effect can hold for all ϕ_0 except for $\phi_0 = 0, \pi$. For other $\phi_r \neq \pi$, we have numerically checked the energy spectrum under PBC and the eigen-modes under OBC, and conclude that the skin effect can expand to all the phase parameters except for $\phi_r = 0$. In fact, for $\phi_r = 0$, we can write down the tight-binding Hamiltonian in the k space as

$$H = - \sum_k 2t \cos k (c_{k\uparrow}^\dagger c_{k\uparrow} - c_{k\downarrow}^\dagger c_{k\downarrow}) + i\gamma \sum_k (c_{k\uparrow}^\dagger c_{k\uparrow} - c_{k\downarrow}^\dagger c_{k\downarrow}) + \Omega_0 \sum_k (-ie^{i\phi_0} 2 \sin k c_{k\uparrow}^\dagger c_{k\downarrow} + H.c.) + \Omega_r \sum_k (c_{k\uparrow}^\dagger c_{k-\pi,\downarrow} + H.c.). \quad (19)$$

We see that the last term couples k to $k-\pi$, and in the basis $\psi = (c_{k-\pi,\uparrow}, c_{k-\pi,\downarrow}, c_{k,\uparrow}, c_{k,\downarrow})^T$, we have $H = \sum_k \psi^\dagger h(k) \psi$ with $h(k)$ a 4×4 matrix. The diagonalization of $h(k)$ gives rise to the eigen-spectrum under PBC. In Fig. 8, we show two typical energy spectra in the complex energy plane for $\gamma < \Omega_r$ and $\gamma > \Omega_r$ with $\phi_0 = \pi/2$. We see that the PBC spectrum in the complex plane behaves either as two disconnected lines or as two open arcs, but not closed loops. Other ϕ_0 cases shows similar features. Therefore the NHSE does not show up if $\phi_r = 0$.

In Fig. 9 we summarize the existence regions for the NHSE for case-III in the phase plane (ϕ_r, ϕ_0) . It is shown that the skin effect is absent for two discrete points $(\pi, 0)$ and (π, π) and a line at $\phi_r = 0$.

V. Non-Hermitian skin effect under realistic confinements

Here we consider two types of realistic confinements in cold atoms, one is the box-trap potential with clear edges, and the other is the harmonic potential without a clear edge. In the first case, we consider the realistic situation when the edge is not sharp enough, i.e., there is an additional large but finite laser potential on each side of the lattice, see the illustration in Fig. 10(a). To examine the effect of edge imperfection, we have computed the edge-to-edge transport from $i = 1$ to L (P_{LR}) or from $i = L$ to 1 (P_{RL}), when the laser potentials are applied at sites $i = 0$

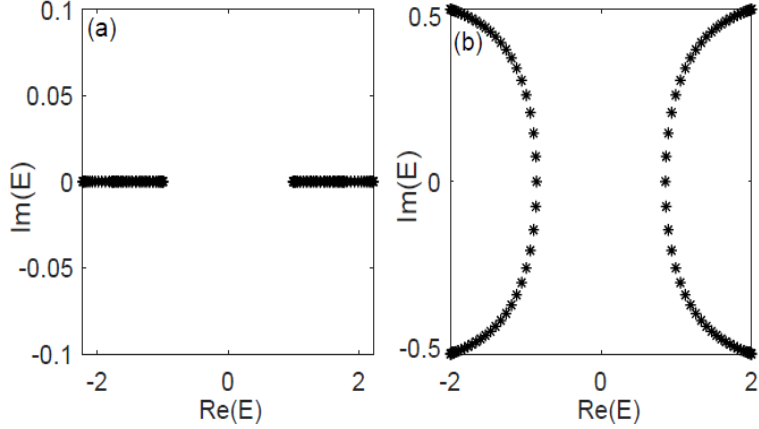


FIG. 8. (Color online) Energy spectrum under periodic boundary condition (PBC) for (a) $\Omega_0 = 0.5$, $\Omega_r = 0.3$, $\gamma = 0.2$ and (b) $\Omega_0 = 0.5$, $\Omega_r = 0.3$, $\gamma = 0.6$. In both cases we take $(\phi_r, \phi_0) = (0, \pi/2)$.

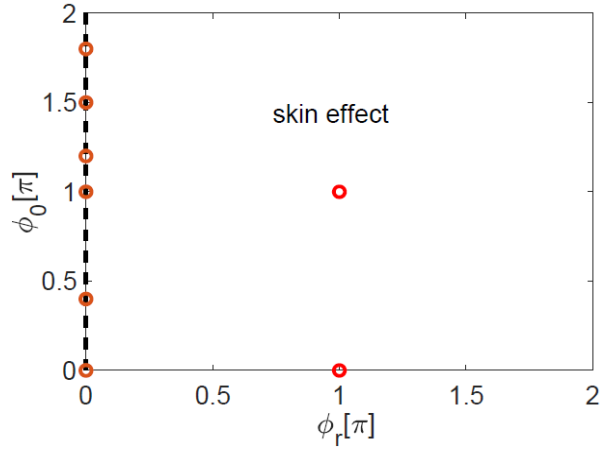


FIG. 9. (Color online) The region of NHSE in the plane of (ϕ_r, ϕ_0) . The red circles at $(\pi, 0)$ and (π, π) , as well as the dashed line at $\phi_r = 0$, denote the parameter regimes for the absence of the non-Hermitian skin effect.

and $L + 1$ with strength V . For simplicity, in our numerics the hopping rate between different sites and all other parameters are taken to be the same as those without the box potential. The results are shown in Fig. 10(b1,b2) for $V = 5t$.

For the first case, we see that the edge-to-edge transport shares qualitatively the same features as those in Fig. 5 of the main text. In the topological phase without NHSE (Fig. 10(b1)), P_{LR} and P_{RL} are identical to each other, and the oscillation frequency decays exponentially with size L . In comparison, the dynamics with NHSE shows obvious directional preference (Fig. 10(b2)), as the localized bulk states contribute significantly.

We now turn to the second case and discuss the manifestation of NHSE in a lattice system under a harmonic trap, $V(x) = V_0 x^2$, where the edge is not well-defined. In our simulation, we take the trap center at the lattice site i_0 and thus there is a local on-site potential $\mu_i = V(i - i_0)^2$ to each site index i , with $V = V_0 a^2$ (a is the lattice spacing). We then consider the expansion dynamics of a particle from the trap center $i = i_0$, see illustration in Fig. 11(a)). To eliminate the difference caused by spin, we consider the initial state as an equal population of $|\uparrow\rangle$ and $|\downarrow\rangle$ at site i_0 , and then examine the probability of finding a particle at site n after an evolution time of τ , defined as

$$n(\tau) \equiv \sum_{\sigma} |\psi_{n,\sigma}(\tau)|^2. \quad (20)$$

In Fig. 11(a1,a2,b1,b2), we show the contour plot of $\rho_n(\tau)$ in the (n, τ) plane for various cases of γ and V parameters. One can see that in the absence of NHSE ($\gamma = 0$ in (a1,a2)), the particle wave function expands from the trap center with equal probabilities to the right- and left-hand sides. In comparison, when the NHSE is present under a finite γ (b1,b2), the expansion shows strong directional preference towards the left-hand side (smaller index) of the lattice.

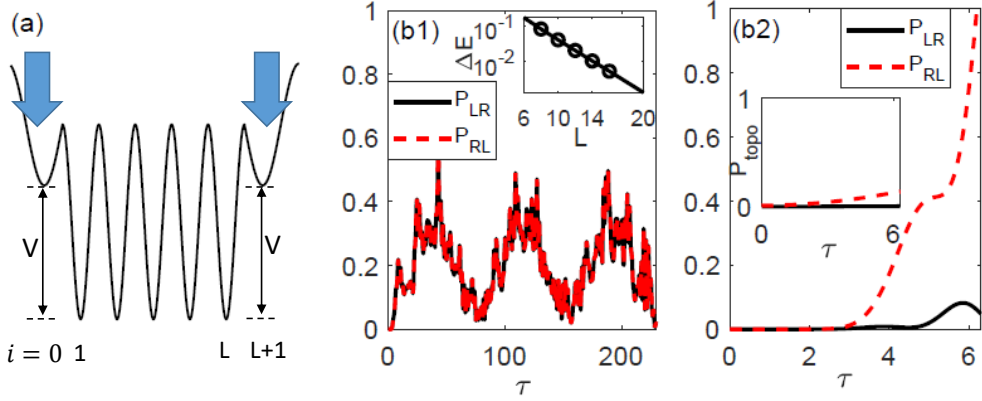


FIG. 10. (Color online) (a) Illustration of the lattice system under a box potential with imperfect edges. (b1,b2) P_{LR} and P_{RL} between lattice sites $i = 1$ and L without (b1) and with (b2) NHSE. Here we take the laser potential $V = 5t$, and all other parameters are identical to Fig. 5 in the main text. The insets of (b1) and (b2) are also the same physical quantities as in the insets of Fig. 5 in the main text.

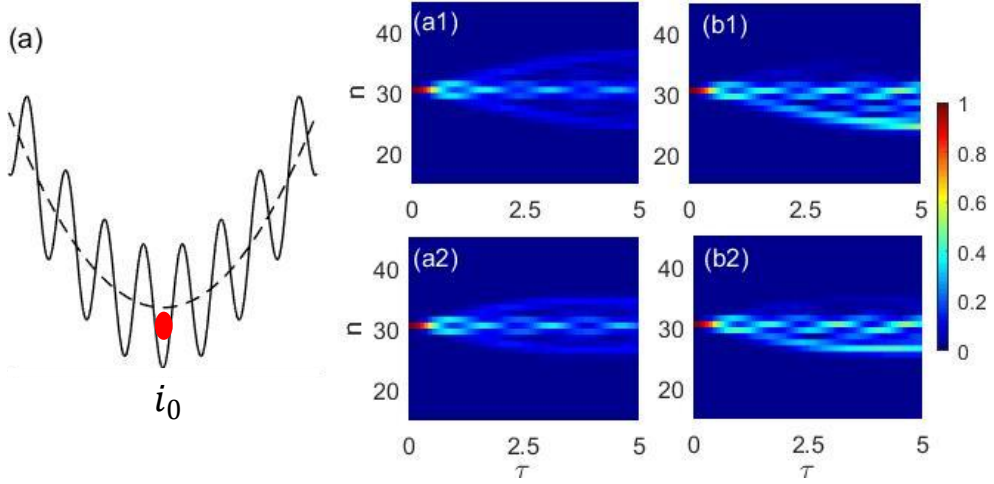


FIG. 11. (Color online) (a) Illustration of the lattice system with an additional harmonic potential. (a1,a2,b1,b2) Contour plot of $\rho_n(\tau)$ in the (n, τ) plane for the bulk dynamics in a harmonic trap. Here we take $\Omega_r = 1, \Omega_0 = 0.5$, and other parameters are $(\gamma, V) = (0, 0.1)$ (a1), $(0, 0.2)$ (a2), $(0.2, 0.1)$ (b1), $(0.2, 0.2)$ (b2). The lattice size is $L = 60$, and the particle is initialized at $i_0 = L/2$ (the trap center).

The probability peak apparently moves to the left-hand side of the trap center at short times, which then saturates at a certain distance to the trap center at longer times. By comparing (a1,b1) and (a2,b2) with different harmonic confinements, we can see that a stronger V will suppress the directional flow, i.e., the off-center displacement of the particle becomes smaller as V increases, whereas the off-center accumulation of population becomes more appreciable. We have also checked that in the absence of the harmonic trap $V = 0$, the expansion peak moves to left-hand side continuously (before getting close to any boundaries). These results show that even there is no sharp edge or boundary, the NHSE can also manifest itself in the bulk dynamics.

* wyiz@ustc.edu.cn

† xlcui@iphy.ac.cn

[1] B. Song, L. Zhang, C. He, T. F. Jeffrey Poon, E. Hajiyev, S. Zhang, X.-J. Liu, G.-B. Jo, “Observation of symmetry-protected topological band with ultracold fermions”, Sci. Adv. 4, eaao4748 (2018).
[2] Z. Ren, D. Liu, E. Zhao, C. He, K. K. Pak, J. Li, G.-B. Jo, “Topological control of quantum states in non-Hermitian spin-orbit-coupled fermions”, arxiv: 2106.04874.